# A nonlinear electroelastic metastructure for broadband wave attenuation

**J. A. Mosquera-Sánchez, C. De Marqui Jr.**
University of São Paulo, São Carlos School of Engineering, Department of Aeronautical Engineering, Avenida João Dagnone, 1100 - Jardim Santa Angelina, 13563-120, São Carlos, Brazil

## Abstract

This paper presents an electroelastic realization of a nonlinear metastructure, based on piezoelectric patches and nonlinear shunt circuits. The nonlinear attachments consist on shunt circuits that feature an inductance and a nonlinear circuit, whose response is proportional to the cube of the electrical current. The piezoelectric layers are placed such that they entirely cover the top and bottom faces of the elastic substrate. The external electrodes are continuously segmented into several parts so as to constitute the electroelastic metastructure, with as many shunt circuits as electrode segments. This paper shows that the interaction among the shunt circuits in the periodic metastructure leverages a chaotic band, in which the resonances of the bare structure are significantly reduced. Numerical simulations based on an electromechanical Euler-Bernoulli finite element and on direct time-domain integration demonstrate the benefit of constituting nonlinear electroelastic metastructures for wave attenuation. Experimental demonstrations confirm the numerical findings.

## 1 Introduction

Currently, linear locally resonant metastructures are at an advanced level of understanding, wherein all their effects on the mechanical wave propagation through solid media are well known [1, 2, 3]. Yet, only a few examples are found on nonlinear metamaterials that take advantage of the complicated yet interesting behaviors for their performance enhancement. Most of the available research in nonlinear metamaterials and metastructures has been devoted to the study of their transmissibility properties, based on wave propagation approaches. On the one hand, one-dimensional nonlinear metamaterials based on Duffing-type oscillators [4, 5], complete cubic-order polynomials [6, 7], and bistable attachments [8, 9], are examples that harness nonlinear resonating attachments in the enhancement of the attenuation band properties, *i.e.* its location, edges, and intensity. On the other hand, an even reduced amount of efforts are currently available that combine the benefits of engineered nonlinearities and piezoelectric metastructures [10, 11, 12, 13, 14]. These studies have demonstrated improved vibration attenuation capabilities and impressive wave propagation features that can be rendered useful even for energy harvesting and insulation applications.

This paper presents numerical and experimental investigations on the transmissibility properties of an one-dimensional nonlinear piezoelectric metastructure, with a focus on piezoelectric resonators featuring positive cubic relationships between the electrical charge and the voltage. The interplay between nonlinear electrical oscillators and negative capacitance (NC) circuits is also addressed to show its positive effects in facilitating the tuning of the piezoelectric attachments in the presence of fixed inductors. A piezoelectric metastructure with 12 nonlinear attachments is modeled by using Euler-Bernoulli electromechanical finite elements [3], and the full matrices are reduced by using an electromechanically coupled Galerkin projection basis [15]. The reduced electromechanical model is solved by using Runge-Kutta (RK)-based, time-domain integration [16, 17, 18], and the steady-state transmissibility curves are compared with experimental results that showed a high agreement between both approaches. In special, it has been seen that flat transmissibilities around the underlying linear bandgap arise when the nonlinear coefficients are set to large values that elucidate strongly nonlinear behaviors, whereas mixed linear (attenuation band) and nonlinear (wave supratransmission and nonlinear reductions) effects are found when the attachments are set to weakly and moderately nonlinear

values.

This paper is organized as follows: Section 2 briefly describes the set of equations of motion for the one-dimensional piezoelectric metastructure through a finite element (FE)-based procedure; Section 3 presents numerical and experimental results of a nonlinear piezoelectric metastructure, where the transmissibility functions are shown to discuss the relevant dynamic behaviors; and Section 4 ends this paper with concluding remarks and future directions on this research.

## 2 Numerical Modeling

Figure 1(a) illustrates an electroelastic unit cell of the nonlinear piezoelectric metastructure, which consists of a homogeneous, slender bending beam to which one single piezoelectric element is bonded onto one of its surfaces. The actual one-directional metastructure is formed after repeating the unit cell several times along one single direction. The structural domains are parameterized by their geometrical and material properties given by the length $l$, width $w$, and thickness $h$; and by the density $\rho$, elastic modulus $c$, and effective one-dimensional piezoelectric parameters $\bar{c}_{11}$ (elastic modulus), $\bar{e}_{31}$ (stress constant), and $\bar{\epsilon}_{33}$ (permittivity component) [19], where the subscripts $s$, $p$ denote substrate and piezoelectric domains, respectively. The continuum is approached by using a Hamiltonian approach, and the equations that govern its dynamical behavior are obtained by following finite element (FE) procedures [3, 20, 21, 22]. Since the host structure is to be subjected to low-amplitude harmonic loads, the mathematical derivations of the elastic domain rely upon linear constitutive relationships, which are valid for both the substrate and the piezoelectric layers.

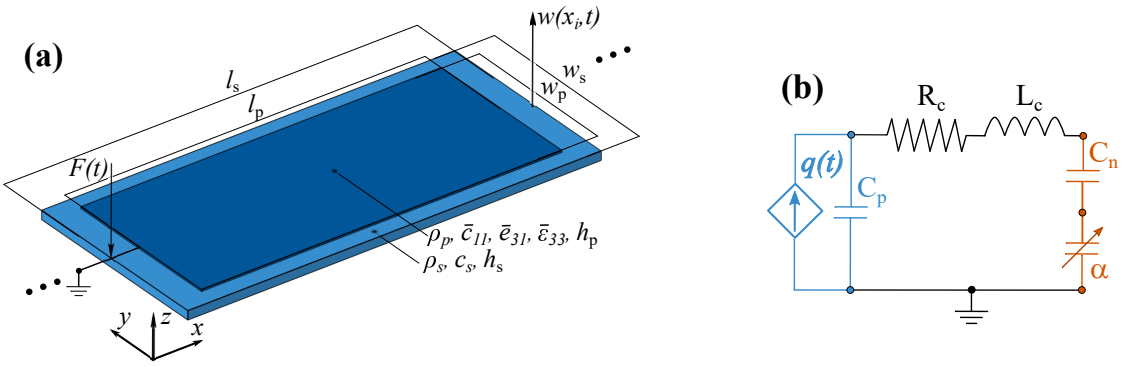


Figure 1: Sketches of the distributed-parameter nonlinear piezoelectric unit cell: (a) 3-D view of the NPMS' unit cell; (b) nonlinear shunt circuit.

The shunt circuit shown in Fig. 1(b) consists of an inductor, $L_c$, a resistor, $R_c$, a negative capacitor, $C_n$, and a nonlinear capacitor with nonlinear coefficient $\alpha$ that presents a cubic voltage-charge relation [23, 24]. As shown in the figure, all the electric components in the external circuit are connected in series form. This external shunt circuit is then connected in parallel with the piezoelectric element, which is mathematically modeled as a controlled current source in parallel to the piezoelement's capacitance.

With the structural and piezoelectric matrices obtained from finite element procedures, the complete set of equations of motion of the electroelastic body that accounts for a single nonlinear shunt circuit can be stated in a matrix form, as follows:

$$\begin{bmatrix} \boldsymbol{M} & \boldsymbol{0} \\ \boldsymbol{0}^t & L_c \end{bmatrix} \begin{Bmatrix} \ddot{\boldsymbol{w}} \\ \ddot{q} \end{Bmatrix} + \begin{bmatrix} \boldsymbol{D} & \boldsymbol{0} \\ \boldsymbol{0}^t & R_c \end{bmatrix} \begin{Bmatrix} \dot{\boldsymbol{w}} \\ \dot{q} \end{Bmatrix} + \begin{bmatrix} \boldsymbol{K} & \boldsymbol{\Theta} \boldsymbol{C}_p^{-1} \\ \boldsymbol{\Theta}^t C_p^{-1} & C_r^{-1} \end{bmatrix} \begin{Bmatrix} \boldsymbol{w} \\ q \end{Bmatrix} + \alpha \boldsymbol{F}_{nl}^D \begin{Bmatrix} \boldsymbol{0} \\ q^3 \end{Bmatrix} = \begin{Bmatrix} \boldsymbol{F} \\ 0 \end{Bmatrix}, \tag{1}$$

where $\boldsymbol{w}$ denote the transverse displacement, and the overdots denote derivatives with respect to time; $\{\boldsymbol{M},\ \boldsymbol{D},\ \boldsymbol{K}\} \in \mathbb{R}^{(n_s \times n_s)}$ are the global mass, damping, and stiffness matrices, respectively, with $n_s$ being

the total number of structural DoF; $\boldsymbol{\Theta} \in \mathbb{R}^{(n_s \times n_e)}$ is the global electromechanical coupling matrix with $n_e$ being the total number of electrical DoF in the FE mesh; $\boldsymbol{C}_p \in \mathbb{R}^{(n_e \times n_e)}$ is the global, diagonal matrix of piezoelectric capacitances; $\boldsymbol{C}_r \in \mathbb{R}^{(n_e \times n_e)}$ is the global, diagonal matrix of *residual* capacitances that results after placing a negative capacitor, $C_n$, in the external shunt circuit as shown in Fig. 1(b); $\boldsymbol{F} \in \mathbb{R}^{(n_s \times 1)}$ is the global vector of structural loads; $\boldsymbol{q} \in \mathbb{R}^{(n_e \times 1)}$ is the global vector of *extracted* electrical charges; $\mathbf{0} \in \mathbf{0}^{n_s \times 1}$ is a null vector; and $\boldsymbol{F}_{nl}^{D} = \left[\left[\mathbf{0}^{n_s \times n_s},\ \mathbf{0}^{n_s \times 1}\right];\left[\mathbf{0}^{1 \times n_s},\ 1\right]\right]$ is the influence coefficient matrix [25] that indicates the position at which the local cubic force is applied into the electroelastic beam. It is worth noticing that the piezoelectric matrices, $\boldsymbol{\Theta}$ and $C_p$, should be reduced by condensing the electrical degrees of freedom [3] as, since the piezoelectric layer is covered with thin and conductive electrodes, it can be safely assumed that all the finite elements belonging to the same piezoelectric element generate the same voltage output. In this way, for the unit-cell case, $\boldsymbol{\Theta}$ becomes a $(n_s \times 1)$-sized vector, while $C_p$ becomes a single scalar value denoting the actual inherent piezoelectric capacitance. This also makes $C_r$ to be a single scalar value denoting the residual capacitance after implementing the negative capacitor in the external series shunt circuit.

To account for $L$ independent shunt circuits, the electrical terms in Eq. 1 can be rewritten as $(L \times L)$-sized diagonal matrices, where $\boldsymbol{L} = diag\,(L_c,\ L_c \ldots\ L_c)$; $\boldsymbol{R} = diag\,(R_c,\ R_c \ldots\ R_c)$; $\boldsymbol{C}_p = diag\,(C_p,\ C_p \ldots\ C_p)$; and $\boldsymbol{C}_r = diag\,(C_r,\ C_r \ldots\ C_r)$. Hence, the equations of motion of the electroelastic metastructure becomes:

$$\begin{bmatrix} \boldsymbol{M} & \mathbf{0} \\ \mathbf{0}^t & \boldsymbol{L} \end{bmatrix} \begin{Bmatrix} \ddot{\boldsymbol{w}} \\ \ddot{\boldsymbol{q}} \end{Bmatrix} + \begin{bmatrix} \boldsymbol{D} & \mathbf{0} \\ \mathbf{0}^t & \boldsymbol{R} \end{bmatrix} \begin{Bmatrix} \dot{\boldsymbol{w}} \\ \dot{\boldsymbol{q}} \end{Bmatrix} + \begin{bmatrix} \boldsymbol{K} & \boldsymbol{\Theta}\boldsymbol{C}_p^{-1} \\ \boldsymbol{\Theta}^t\boldsymbol{C}_p^{-1} & \boldsymbol{C}_r^{-1} \end{bmatrix} \begin{Bmatrix} \boldsymbol{w} \\ \boldsymbol{q} \end{Bmatrix} + \alpha \boldsymbol{F}_{nl}^{D} \begin{Bmatrix} \mathbf{0} \\ \boldsymbol{q}^3 \end{Bmatrix} = \begin{Bmatrix} \boldsymbol{F} \\ \emptyset \end{Bmatrix}, \tag{2}$$

where $F_{nl}^{D} = \left[\left[\mathbf{0}^{n_s \times n_s},\ \mathbf{0}^{(n_s+L) \times 1}\right];\left[\mathbf{0}^{1 \times (n_s+L)},\ \boldsymbol{I}^{L \times L}\right]\right]$; $\boldsymbol{q} \in \mathbb{R}^{L \times 1}$ is the vector of electrical charges; $\mathbf{0} \in \mathbf{0}^{n_s \times L}$; and $\emptyset \in \mathbf{0}^{L \times 1}$. Notice that, for the piezoelectric metastructure case, $\boldsymbol{\Theta}$ becomes a $(n_s \times L)$-sized matrix.

## 2.1 Model reduction

Although the FE model for the nonlinear piezoelectric metastructure stated in Eq. 2 provides a high level of accuracy, even with matrices that are several times smaller than those obtained through full 3D FE models, nonlinear time- and frequency-domain computational analyses may still be infeasible in affordable times due to their relatively large size. Therefore, the set of equations of motion in Eq. 2 is now reduced by using the *electromechanically coupled* Galerkin projection [15], where the electromechanical modal basis is determined by solving the following generalized eigenvalue problem:

$$\left[-\varpi^2 \widetilde{\boldsymbol{M}} + \widetilde{\boldsymbol{K}}\right] \boldsymbol{\Phi} = 0, \tag{3}$$

where $(\varpi,\ \Phi)$ are the eigenvalues and eigenvectors, with $\Phi_i = [\Phi'_{si},\ \Phi'_{Li}]$ being the $i$-th eigenvector composed of $n_s$ mechanical degrees of freedom and by $L$ electrical degrees of freedom. This makes $\boldsymbol{\Phi} \in \mathbb{R}^{(n_s+L) \times P}$, with $P$ being the number of elastic modes to be retained in the modal basis.

The Galerkin projection given by $\boldsymbol{W} = \boldsymbol{\Phi}\overline{\boldsymbol{w}}(t)$, together with its time derivatives, are substituted into Eq. 2, which, by premultiplying its first line by $\boldsymbol{\Phi}^t$, gives the following reduced system of equations, as follows:

$$\begin{bmatrix} \boldsymbol{\mathcal{M}} & \mathbf{0} \\ \mathbf{0}^t & \boldsymbol{L} \end{bmatrix} \begin{Bmatrix} \ddot{\overline{\boldsymbol{w}}} \\ \ddot{\boldsymbol{q}} \end{Bmatrix} + \begin{bmatrix} \boldsymbol{\mathcal{D}} & \mathbf{0} \\ \mathbf{0}^t & \boldsymbol{R} \end{bmatrix} \begin{Bmatrix} \dot{\overline{\boldsymbol{w}}} \\ \dot{\boldsymbol{q}} \end{Bmatrix} + \begin{bmatrix} \boldsymbol{\mathcal{K}} & \overline{\Theta}\boldsymbol{C}_p^{-1} \\ \boldsymbol{C}_p^{-1}\overline{\Theta}^t & \boldsymbol{C}_r^{-1} \end{bmatrix} \begin{Bmatrix} \overline{\boldsymbol{w}} \\ \boldsymbol{q} \end{Bmatrix} + \alpha \boldsymbol{F}_{nl}^{D} \begin{Bmatrix} \mathbf{0} \\ \boldsymbol{q}^3 \end{Bmatrix} = \begin{Bmatrix} \boldsymbol{\mathcal{F}} \\ \emptyset \end{Bmatrix}, \tag{4}$$

where $\mathbf{0} \in \mathbf{0}^{P \times L}$; $F_{nl}^{D} = \left[\left[\mathbf{0}^{P \times P},\ \mathbf{0}^{(P+L) \times 1}\right];\left[\mathbf{0}^{1 \times (P+L)},\ \boldsymbol{I}^{L \times L}\right]\right]$; and:

$$\boldsymbol{\mathcal{M}} = \boldsymbol{\Phi}^t\widetilde{\boldsymbol{M}}\boldsymbol{\Phi};\quad \boldsymbol{\mathcal{D}} = \boldsymbol{\Phi}^t\widetilde{\boldsymbol{D}}\boldsymbol{\Phi};\quad \boldsymbol{\mathcal{K}} = \boldsymbol{\Phi}^t\widetilde{\boldsymbol{K}}\boldsymbol{\Phi};\quad \overline{\boldsymbol{\Theta}} = \boldsymbol{\Phi}^t\boldsymbol{\Theta};\quad \boldsymbol{\mathcal{F}} = \boldsymbol{\Phi}^t\boldsymbol{F}, \tag{5}$$

The system of equations of motion stated in Eq. 4 is now compactly rewritten as follows:

$$\overline{\boldsymbol{M}}\ddot{\overline{\boldsymbol{z}}} + \overline{\boldsymbol{D}}\dot{\overline{\boldsymbol{z}}} + \overline{\boldsymbol{K}}\overline{\boldsymbol{z}} + \alpha\boldsymbol{F}_{nl}^{D}\overline{\boldsymbol{z}}^{3} = \overline{\boldsymbol{F}}, \tag{6}$$

where $\overline{\boldsymbol{z}} = [\overline{\boldsymbol{w}},\ \boldsymbol{q}]^t$ is the state vector expressed in both modal and electrical coordinates.

# 3 Numerical and Experimental Results

The steady-state transmissibility functions of a finite nonlinear piezoelectric metastructure are presented and discussed in this Section through numerical and experimental results.

Figure 2 illustrates the investigated one-dimensional metastructure, with geometry and constituent material parameters as reported in Table 1. Fig. 2(a) shows the top view of the metastructure's numerical model, while Fig. 2(b) displays the laboratory implementation of the metastructure with the nonlinear circuits, each of them featuring a fixed 60 H inductor (Hammond Manufacturing, ref. 546-156C). The piezoelectric metastructure features a total of 12 unit cells. Additional geometrical and material details for the entire metastructure are given next. The Rayleigh damping coefficients are updated to $b_1 = 1.0\ \text{s}^{-1}$, and $b_2 = 1.1 \times 10^{-5}$ s. Two homogeneous bare waveguides with lengths $l_{s1} = 234.1 \times 10^{-3}$ m, and $l_{s3} = 229.2 \times 10^{-3}$ m, are attached to both extremes of the metastructure, as shown in Fig. 2, which together with the beam portion endowed with the piezo elements (beam portion of length $l_{s2}$) becomes 1.096 m in length ($l_{s1} + l_{s2} + l_{s3}$ in Fig. 2).

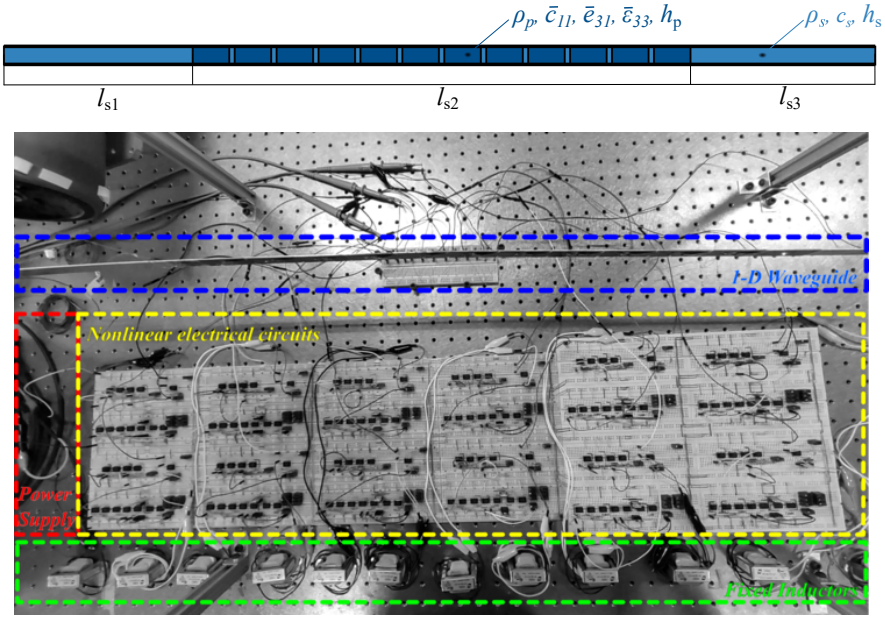


Figure 2: One-dimensional nonlinear piezoelectric metastructure: (a) top view of the structure's sketch; (b) laboratory implementation of the metastructure: workbench's top view including the 12 nonlinear shunt circuits.

## 3.1 Setup of the experimental workbench

Figure 3(a) illustrates the workbench used to obtain the transmissibility measurements from the actual nonlinear piezoelectric metastructure, while Figure 3(b) displays a close-up of one single electrical circuit. The workbench is composed of a closed-loop excitation system, driven by the LMS.Random Control software that controls a 16-input, 2-output LMS.Scadas acquisition system, a electrodynamic shaker with power amplifier set in current mode that excites the metastructure at its left end, and a pair of high-sensitivity accelerometers (100 m$g$ with $g = 9.81\ \text{m.s}^{-2}$), each of them being placed onto the free beam ends. As

Table 1: Geometrical and material parameters of the piezoelectric unit cell (Metastructure: 12 unit cells).

| **Parameter** | **Value** | **Parameter** | **Value** |
|---|---|---|---|
| Substrate length | $52.72 \times 10^{-3}$ m | PZT length | $45.97 \times 10^{-3}$ m |
| Substrate width | $24.85 \times 10^{-3}$ m | PZT width | $24.85 \times 10^{-3}$ m |
| Substrate thickness | $1.10 \times 10^{-3}$ m | PZT compliance, $s_{11}$ | $16.40 \times 10^{-12}$ 1/Pa |
| Substrate Young's modulus | $68.30 \times 10^{9}$ Pa | PZT electromech. coupling, $d_{31}$ | $-171.00 \times 10^{-12}$ C/N |
| Substrate density | $2.80 \times 10^{3}$ kg/m$^3$ | PZT permittivity, $\varepsilon_{33}$ | $15.05 \times 10^{-9}$ F/m |
| PZT thickness | $0.24 \times 10^{-3}$ m | PZT density | $7.75 \times 10^{3}$ kg/m$^3$ |
| Mass damping parameter, $b_1$ | 1.50 1/s | Stiffness damping parameter, $b_2$ | $7.50 \times 10^{-7}$ s |

shown in Figs. 3 and 4, the shunt circuits rely on operational amplifiers (Texas Instruments OPA551) that are powered with a $\pm 32$ VDC source. The system is excited by using random signals that are provided by the LMS.Random Control software, with an amplitude level of $1 \times 10^{-3}$ $g$ across the entire excitation bandwidth. The excitation bandwidth was defined between 0.1 Hz and 200 Hz, and the duration of each measurement was defined as 3600 s to obtain one single FRC, for each case of nonlinear coefficient.

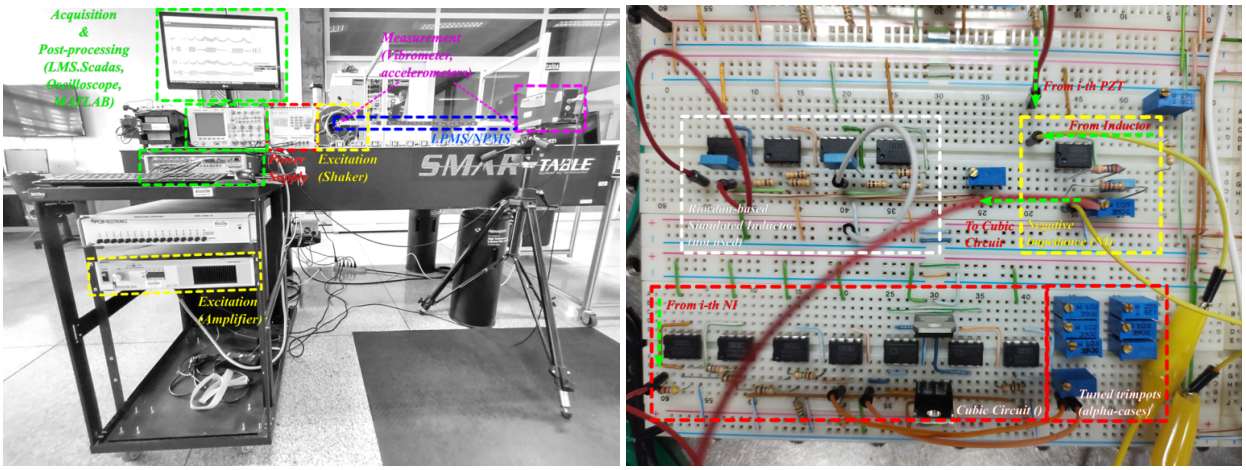


Figure 3: (a) Experimental setup for measurements; (b) image of one single nonlinear analog circuit.

Figure 4 illustrates the electrical scheme that corresponds to the circuit shown in Figure 3(b). The fixed inductor is modeled as a pure inductance in series with a resistance that accounts for the internal losses. From the twelve inductors used in the experiments, a mean resistance value of 2700 $\Omega$ was estimated. Such a high inductor's real impedance was compensated by using a negative impedance circuit, which features a real negative component given by resistor $R_d$, and an imaginary negative component given by capacitor $C_c$, the latter one actually being the negative capacitance that is formed with resistors $R_{a3} = R_{a3c} + R_{a3m}$ [24] and $R_{a4}$.

## 3.2 Setup of the numerical simulations

The continuum was discretized into 120 FEs, which yielded structural matrices of size $242 \times 242$. In the bandwidth of interest (0.1 Hz to 200 Hz), 9 flexible modes and 2 rigid-body modes have been found and kept for composing the modal basis. For the proper representation of the antiresonances, 19 additional flexible modes were added to the Galerkin projection basis. The lowest SC resonant frequency was found as $\omega_{sc,1} = 5.04$ Hz, whereas the lowest OC mode was found as $\omega_{oc1} = 5.14$ Hz. This gives a generalized electromechanical coupling, $K^2_{eff}$, of 0.20. The piezoelectric capacitance of each piezoelement was obtained as $C_p = 52.29 \times 10^{-9}$ F.

The electrical parameters for the numerical simulations were obtained from the experimental measurements. The inductances were numerically adjusted at 39 H ($L_c$) and 200 $\Omega$ ($R_c$), and the NC and nonlinear coef-

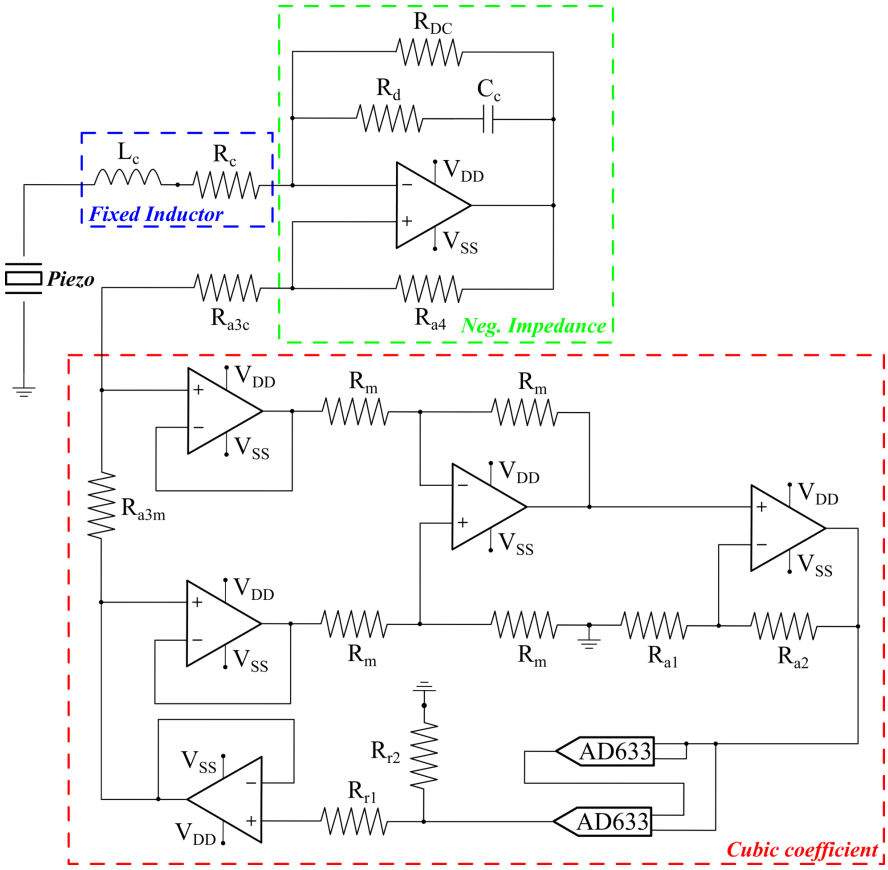


Figure 4: Electrical diagram of the nonlinear shunt circuit.

ficients were directly taken from the experimental results. Since the experimental inductors are fixed, the desired target frequency ($w_t = 100$ Hz) for the attenuation bandgap was attained by using the residual capacitance provided by the negative capacitors. The desired target frequency at 100 Hz was experimentally attained by setting all the negative capacitors to provide the overall effect of $\mu = -0.3025$, where:

$$\mu = \frac{C_p}{C_n}, \tag{7}$$

in which $\mu$ is the residual capacitance rate. Since the NC is placed in series with the piezoelectric capacitance, *cf.* Fig. 1(b), the *residual capacitance*, $C_r$ should be calculated as follows:

$$C_r = \frac{\boldsymbol{C}_p C_n}{\boldsymbol{C}_p + C_n}, \tag{8}$$

which enables the calculation of the attachments' target frequency with given fixed inductors ($L_c$), by using:

$$w_t = \frac{1}{\sqrt{C_r L_c}}. \tag{9}$$

With the electrical parameters properly set, the electromechanically coupled and reduced matrices were submitted to the time-domain integration routine using MATLAB's `ode113` function, with absolute and relative error criteria set equal to $1 \times 10^{-9}$. A point excitation of amplitude $F_m = 5 \times 10^{-02}$ N was imparted to the numerical model, which provided the same amplitudes seen during the experiments. All the initial conditions of both the structural (displacements and velocities) and electrical (electrical charges and currents) DoF were set equal to zero. With a resolution of 0.1 Hz across the bandwidth of interest, 2000 periods of the input harmonic load were integrated for each discrete input frequency (2000 discrete frequencies). The sets of equations of motion were integrated with the aid of a large high-performance computer. The RMS

value of the last quarter of the displacement and velocity time histories taken at both ends of the beam were considered as the frequency-response curves. The transmissibility functions were eventually calculated by dividing the mechanical output at the free right end by the mechanical input at the free left end.

### 3.3 Results

The transmissibility results of the nonlinear piezoelectric metastructure considering five levels of nonlinearity ($\alpha = 5 \times 10^{17}$, $1 \times 10^{18}$, $5 \times 10^{18}$, $1 \times 10^{19}$, and $5 \times 10^{19}$) and negative capacitances set equal to $\mu = -0.3025$ are shown in Figs. 5. The numerical results are illustrated by using continuous, bold lines, while the experimental results are plotted on top of the numerical ones by using dashed, thin lines with circle markers.

The first plot at the upper left corner of the Figure shows the system dynamics when at open-circuit condition, *i.e.* without shunt circuits, which evidences an excellent agreement between the numerical and experimental results. This validates the accuracy of the structural and electromechanical matrices obtained through the finite-element modeling procedures for the metastructure considering 12 piezo elements and the two attached bare waveguides.

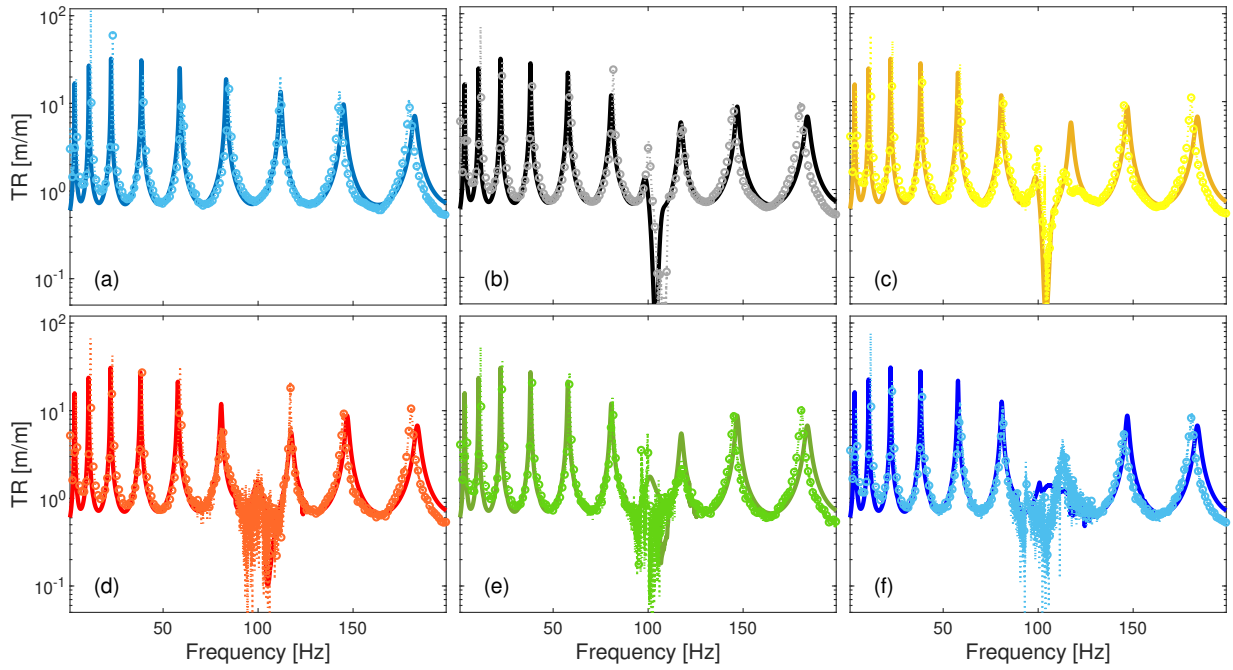


Figure 5: NPMS transmissibility functions with $\mu = -0.3025$, for a set of $\alpha$ values. Continuous lines show numerical results and dashed lines with circled markers illustrate experimental results. Legend: **OC**: —; $\boldsymbol{\alpha}_1 = 5 \times 10^{17}$: —; $\boldsymbol{\alpha}_2 = 1 \times 10^{18}$: —; $\boldsymbol{\alpha}_3 = 5 \times 10^{18}$: —; $\boldsymbol{\alpha}_4 = 1 \times 10^{19}$: —; $\boldsymbol{\alpha}_5 = 5 \times 10^{19}$: —.

The second and third plots in the first row of Fig. 5 show the system dynamics with weakly nonlinear attachments. The second plot displays the quasi-linear behaviors, where a linear, disorder-less attenuation band is seen around the desired target frequency, $\omega_t \approx 100$ Hz. It is worth noticing that the electromechanical coupling for $\mu = -0.3025$ is almost the same as if the attachments did not have NCs, which yields an attenuation band with normalized bandwidth of $\Delta\Omega = 1.74$. The visual comparison between the numerical and experimental curves reflects an excellent agreement between the results. Moreover, some experimentally obtained attenuations imparted to the transmissibility peak immediately located at the right side of the linear attenuation band have not been properly estimated by the numerical model (*cf.* Fig. 5(c)), yet the predictions made for the two nonlinear cases being considered in this paragraph are quite accurate in terms of the overall peak amplitudes and frequency regions at which the metastructure effects arise.

From the second $\alpha$ case onwards, both experimental and numerical results show incremental shifts of the left cutoff frequency to higher frequencies. The moderately nonlinear cases given by $\alpha_3$ and $\alpha_4$ present

good agreement between the numerical and experimental results. For the cases $\alpha_3$ and $\alpha_4$, a quite small attenuation band is still predicted by the numerical model, which is also experimentally verified, *cf.* Fig. 5(d) and (e), respectively. For the strongest $\alpha$ case shown in Fig. 5(f), the numerical model does not predict an attenuation band anymore, but instead a bandwidth with unitary transmissibility, which is mostly verified by the experimental result, except from a slightly large peak seen around 125 Hz that was not predicted by the numerical model. This behavior may indicate that the experimental system should be measured with an even slower acquisition pace, *i.e.* with longer random excitations, to actually converge to the steady state.

The multimode attenuation feature becomes apparent as from the nonlinear cases given by $\alpha_3$ onwards, *cf.* second row of Fig. 5. In particular, cases $\alpha_4$ and $\alpha_5$, *i.e.*, Figs. 5(e) and (f), respectively, are experimentally seen to provide large attenuations around the transmissibility peaks located between 100 Hz and 150 Hz. When these results are superposed onto the quasi-linear results, the multimode attenuation feature becomes notably evident. The flat transmissibility response around the region of the underlying linear bandgap is given by the nonlinear wave supratransmission phenomenon [26, 27] and nonlinear distortions around the transmissibility peaks under strongly nonlinear coefficients [28, 29]. The mixed effects of nonlinear wave supratransmission and attenuations, and the existence of the linear bandgap, are seen when the nonlinear coefficients are set such that weakly and moderately nonlinear regimes are elucidated in the metastructure.

Next directions are given to investigate the effect of the negative capacitors, close to their stability bound, in terms of the electromechanical coupling enhancement and reduction of the piezoelectric capacitance, in order to cast the present Duffing-like nonlinear piezoelectric metastructure into a Nonlinear Energy Sink (NES)-like one, with improved dynamics and wave propagation features. Figure 6 shows the numerical transmissibility considering $\mu = -0.80$. As the nonlinear coefficient increases, the range of low transmissibiity also increases.

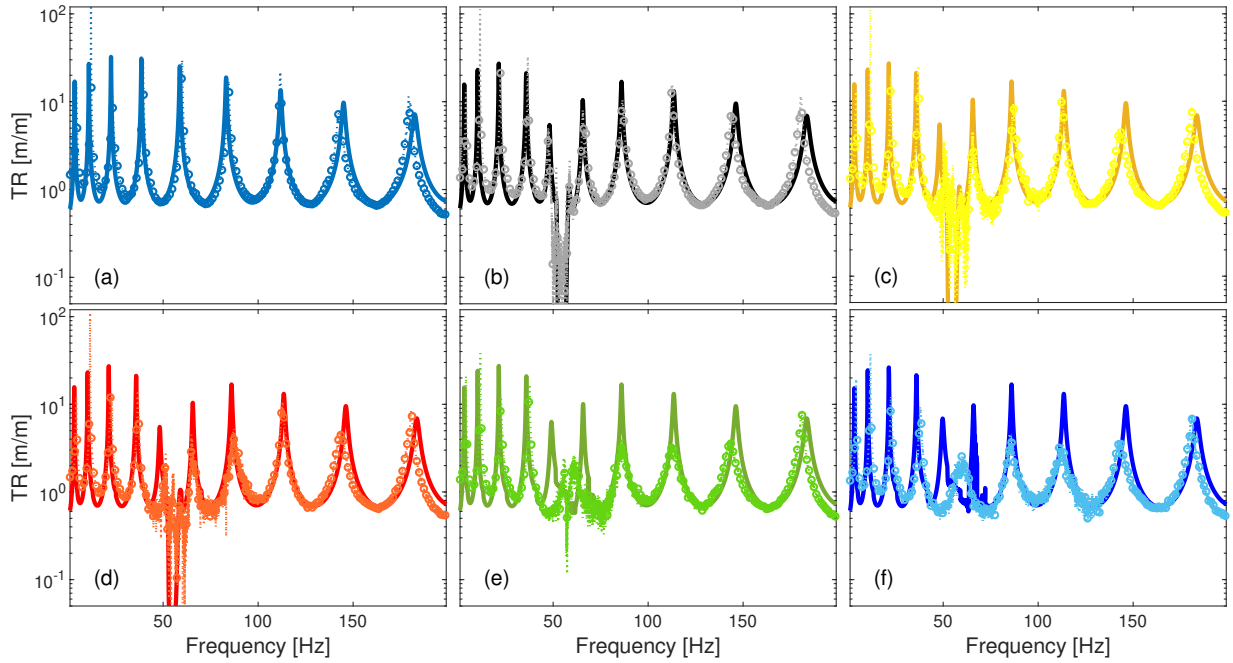


Figure 6: NPMS transmissibility functions with $\mu = -0.8000$, for a set of $\alpha$ values. Continuous lines show numerical results and dashed lines with circled markers illustrate experimental results. Legend: **OC**: —; $\boldsymbol{\alpha}_1 = 1 \times 10^{19}$: —; $\boldsymbol{\alpha}_2 = 5 \times 10^{19}$: —; $\boldsymbol{\alpha}_3 = 1 \times 10^{20}$: —; $\boldsymbol{\alpha}_4 = 5 \times 10^{20}$: —; $\boldsymbol{\alpha}_5 = 1 \times 10^{21}$: —.

# 4 Conclusions

This paper reported the dynamical effects leveraged by introducing nonlinear shunt circuits in one-dimensional locally resonant piezoelectric metastructures. A bending beam endowed with 12 piezoelectric elements under several strengths of nonlinearity and negative capacitances was numerically and experimentally addressed. The nonlinear piezoelectric metastructure was first modeled by using an electromechanical beam finite element. The nonlinear circuits were modeled by using the physical laws that govern the voltage in each electrical component. After using an electromechanically coupled Galerkin projection, the reduced models were submitted to Runge-Kutta-based time-domain integration under harmonic excitations. Linear and nonlinear frequency responses, for a set of nonlinear coefficients that leverage weakly, moderately, and strongly nonlinear regimes, were discussed in the presence of negative capacitances. The comparisons between numerical and experimental results evidence good agreement between both approaches.

The careful setting of the electrical parameters during the experimental campaign enabled linear and quasi-linear, disorder-less attenuation bands that were confirmed by the numerical model. The five practiced levels of nonlinearity showed incremental shifts of the left-side attenuation band cutoff frequency toward high frequencies, to the extent that the underlying linear attenuation band became dominated by nonlinear wave supratransmission. The moderately and strongly nonlinear regimes also elucidated multimode attenuation capabilities. Although some minor differences between the numerical and experimental results were seen in terms of predicting the experimentally attained attenuations, the numerical model proved largely useful to study both linear and nonlinear behaviors of the nonlinear piezoelectric metastructure, even under weakly, moderately, or strongly nonlinear regimes.

# Acknowledgements

This research is funded by the São Paulo State Research Foundation, FAPESP, Brazil, through grants 2018/14546-9, 2018/15894-0, and 2020/01608-6. The authors gratefully acknowledge the computational resources of the Center for Mathematical Sciences Applied to Industry, CeMEAI, of the *Instituto de Ciências Matemáticas e de Computação*, ICMC/USP-SC, funded by FAPESP (grant 2013/07375-0).

# References

[1] C. C. Claeys, E. Deckers, B. Pluymers, and W. Desmet, "A lightweight vibro-acoustic metamaterial demonstrator: numerical and experimental investigation," *Mechanical Systems and Signal Processing*, vol. 70 - 71, no. 2016, pp. 853 – 880, 2016.

[2] L. Y. M. Sampaio, G. K. Rodrigues, J. A. Mosquera-Sánchez, C. De Marqui, and L. P. R. Oliveira, "Membrane smart metamaterials for unidirectional wave propagation problems," *Journal of Sound and Vibration*, vol. 512, p. 116374, Jul. 2021.

[3] R. L. Thomes, J. A. Mosquera-Sánchez, and C. De Marqui Jr., "Bandgap widening by optimized disorder in one-dimensional locally resonant piezoelectric metamaterials," *Submitted to: Journal of Sound and Vibration*, vol. -, pp. –, 2021.

[4] B. S. Lazarov and J. S. Jensen, "Low-frequency band gaps in chains with attached non-linear oscillators," *International Journal of Non-Linear Mechanics*, vol. 42, pp. 1186 – 1193, 2007.

[5] X. Fang, J. Wen, J. Yin, D. Yu, and Y. Xiao, "Broadband and tunable one-dimensional strongly nonlinear acoustic metamaterials - theoretical study," *Physical Review E*, vol. 94, p. 052206, 2016.

[6] P. B. Silva, M. J. Leamy, M. G. D. Geers, and V. G. Kouznetzova, "Emergent subharmonic band gaps in nonlinear locally resonant metamaterials induced by autoparametric resonance," *Physical Review E*, vol. 99, no. 063003, 2019.

[7] V. Zega, P. B. Silva, M. G. D. Geers, and V. G. Kouznetzova, "Experimental proof of emergent subharmonic attenuation zones in a nonlinear locally resonant metamaterial," *Scientific Reports*, vol. 10, no. 10.1038/s41598-020-68894-3, pp. 1 – 11, 2020.

[8] Y. Xia, M. Ruzzene, and A. Erturk, "Dramatic bandwidth enhancement in nonlinear metastructures via bistable attachments," *Applied Physics Letters*, vol. 114, no. doi: 10.1063/1.5066329, p. 5pp, 2019.

[9] Y. Xia, M. Ruzzene, and A. Erturk, "Bistable attachments for wideband nonlinear vibration attenuation in a metamaterial beam," *Nonlinear Dynamics*, p. 12pp, 2020.

[10] B. Bao, D. Guyomar, and M. Lallart, "Vibration reduction for smart periodic structures via periodic piezoelectric arrays with nonlinear interleaved-switched electronic networks," *Mechanical Systems and Signal Processing*, vol. 82, pp. 230–259, 2017.

[11] Y. Zheng, Z. Wu, X. Zhang, and K. W. Wang, "A piezo-metastructure with bistable circuit shunts for adaptive nonreciprocal wave transmission," *Smart Materials and Structures*, vol. 28, p. 045005, 2019.

[12] M. Bukhari and O. Barry, "Simultaneous energy harvesting and vibration control in a nonlinear metastructure: a spectro-spatial analysis," *Journal of Sound and Vibration*, vol. 473, p. 115215, 2020.

[13] Z. Chen, Y. Xia, J. He, Y. Xiong, and G. Wang, "Elastic-electro-mechanical modeling and analysis of piezoelectric metamaterial plate with a self-powered synchronized charge extraction circuit for vibration energy harvesting," *Mechanical Systems and Signal Processing*, vol. 143, no. 106824, pp. 1–18, 2020.

[14] Z. Chen, W. Zhou, and C. W. Lim, "Active control for acoustic wave propagation in nonlinear diatomic acoustic metamaterials," *International Journal of Non-linear Mechanics*, vol. 125, no. 103535, p. 9pp, 2020.

[15] W. Larbi and J.-F. Deu, "Reduced order finite element formulations for vibration reduction using piezoelectric shunt damping," *Applied Acoustics*, vol. 147, pp. 111–120, 2019.

[16] Y.-W. Zhang, Y.-N. Lu, W. Zhang, Y.-Y. Teng, H.-X. Yang, T.-Z. Yang, and L.-Q. Chen, "Nonlinear energy sink with inerter," *Mechanical Systems and Signal Processing*, vol. 125, pp. 52–64, 2019.

[17] W. Zhang, J. H. Yang, Y. F. Zhang, and S. W. Yang, "Nonlinear transverse vibrations of angle-ply laminated composite piezoelectric cantilever plate with four-modes subjected to in-plane and out-of-plane excitations," *Engineering Structures*, vol. 198, no. 109501, p. 21pp, 2019.

[18] S. F. Lu, Y. Jiang, W. Zhang, and X. J. Song, "Vibration suppression of cantilevered piezoelectric laminated composite rectangular plate subjected to aerodynamic force in hygrothermal environment," *European Journal of Mechanics / A Solids*, vol. 83, no. 104002, p. 23pp, 2020.

[19] C. Sugino, S. Leadenham, M. Ruzzene, and A. Erurk, "An investigation of electroelastic bandgap formation in locally resonant piezoelectric metastructures," *Smart Materials and Structures*, vol. 26, no. 055029, p. 10pp, 2017.

[20] M. Petyt, *Introduction to Finite Element Vibration Analysis*. Cambridge University Press, 1988.

[21] C. De Marqui Jr., A. Erturk, and D. J. Inman, "An electromechanical finite element model for piezoelectric energy harvester plates," *Journal of Sound and Vibration*, vol. 327, pp. 9 – 25, 2009.

[22] M. F. Lumentut and I. M. Howard, "Electromechanical finite element modelling for dynamic analysis of a cantilevered piezoelectric energy harvester with tip mass offset under base excitations," *Smart Materials and Structures*, vol. 23, no. 095037, p. 24pp, 2014.

[23] B. Zhou, F. Thouverez, and D. Lenoir, "Essentially nonlinear piezoelectric shunt circuits applied to mistuned bladed disks," *Journal of Sound and Vibration*, vol. 333, pp. 2520 – 2542, 2014.

[24] T. M. P. Silva, M. A. Clementino, C. De Marqui Jr., and A. Erturk, "An experimentally validated piezoelectric nonlinear energy sink for wideband vibration attenuation," *Journal of Sound and Vibration*, vol. 437, pp. 68–78, 2018.

[25] B. Bergeot and S. Bellizzi, "Steady-state regimes prediction of a multi-degree-of-freedom unstable dynamical system coupled to a set of nonlinear energy sinks," *Mechanical Systems and Signal Processing*, vol. 131, pp. 728–750, 2019.

[26] B. Yousefzadeh and A. Srikantha Phani, "Energy transmission in finite dissipative nonlinear periodic structures from excitation within a stop band," *Journal of Sound and Vibration*, 2015.

[27] J. A. Mosquera-Sánchez and C. De Marqui Jr., "Dynamics and wave propagation in nonlinear piezoelectric metastructures," *Nonlinear Dynamics*, vol. 105, pp. 2995 – 3023, Aug. 2021.

[28] X. Fang, J. Wen, J. Yin, and D. Yu, "Wave propagation in nonlinear metamaterial multi-atomic chains based on homotopy method," *AIP Advances*, vol. 6, p. 121706, 2016.

[29] X. Fang, J. Wen, B. Bonello, J. Yin, and D. Yu, "Ultra-low and ultra-broad-band nonlinear acoustic metamaterials," *Nature Communications*, pp. DOI: 10.1038/s41 467–017–00 671–9, 2017.